

An Iron Bis(carbene) Catalyst for Low Overpotential CO₂ Electroreduction to CO: Mechanistic Insights from Kinetic Zone Diagrams, Spectroscopy, and Theory

Sergio Gonell,^{1,2,*} Eric A. Assaf,¹ Julio Lloret-Fillol,^{2,3,*} Alexander J. M. Miller^{1*}

¹ University of North Carolina at Chapel Hill, Chapel Hill, North Carolina 27599-3290, United States

² Institute of Chemical Research of Catalonia (ICIQ), The Barcelona Institute of Science and Technology, Avinguda Països Catalans, 16, 43007 Tarragona, Spain

³ Catalan Institution for Research and Advanced Studies (ICREA), Passeig Lluís Companys, 23, 08010 Barcelona, Spain

Present Address for S.G. Institute of Advanced Materials (INAM). Universitat Jaume I. Av. Vicente Sos Baynat s/n., 12071 Castelló (Spain)

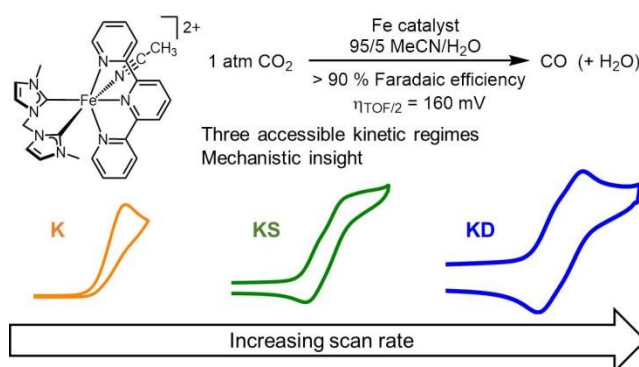
Corresponding Author E-mail Addresses:

sgonell@uji.es (S.G.)

jlloret@iciq.es (J.LI-F.)

ajmm@email.unc.edu (A.J.M.M.)

TOC Graphic



Abstract

A common challenge in molecular electrocatalysis is the relationship between maximum activity and the overpotential required to reach that rate, with faster catalysts incurring higher overpotentials. This work follows a strategy based on independent tuning of ligands in the primary coordination sphere to discover a previously unreported iron catalyst for CO₂ reduction with higher activity than similar complexes while maintaining the same

overpotential. Iron complexes bearing the bis-N-heterocyclic carbene ligand (methylenebis(*N*-methylimidazol-2-ylidene, bis-mim) and a redox active 2,2':6',2''-terpyridine (tpy) ligand were synthesized and found to catalyze the selective reduction of CO₂ to CO at low overpotential with water as the proton source. Mechanistic studies based on kinetic zone diagrams, spectroscopy, and computation enable comparisons with a previously studied pyridyl-carbene analogue. Changing the bidentate ligand donor ability accelerates catalysis at the same overpotential, and changes the nature of the turnover-limiting step of the reaction.

Keywords:

CO₂ reduction, electrocatalysis, iron, carbene ligand, mechanistic studies

Introduction

The electrochemical reduction of CO₂ holds promise for the sustainable synthesis of fuels and chemicals, but faces challenges in terms of selectivity and achieving high activity at low overpotentials. Transition metal complexes are promising candidates for CO₂ reduction catalysis. The synthetic tunability and relative ease of mechanistic analysis of molecular catalysts compared with heterogeneous catalysts can elucidate structure–function relationships and provide guidance on how to tune rate, overpotential, and selectivity in CO₂ electroreduction.^{1–7}

One fruitful approach to achieve high activity at low overpotential involves installing functionality into the *secondary* coordination sphere of the catalyst (Figure 1).^{8–10} Complexes bearing pendent amine, alcohol, ether, or cationic alkylammonium groups are exceptional catalysts for H₂ evolution and CO₂ reduction.^{11–20} We have recently examined an alternative and complementary strategy based on careful composition of the *primary* coordination sphere (Figure 1). The hypothesis is that by pairing one “redox-active” ligand with another strongly electron-donating but “redox-inactive” ligand *trans* to the CO₂ binding coordination site, we can separately tune the onset potential of catalysis and the rate of the limiting chemical step(s). This approach could avoid a common pitfall of primary coordination sphere tuning, where increased activity comes at the expensive of higher overpotentials required to maximize rate.

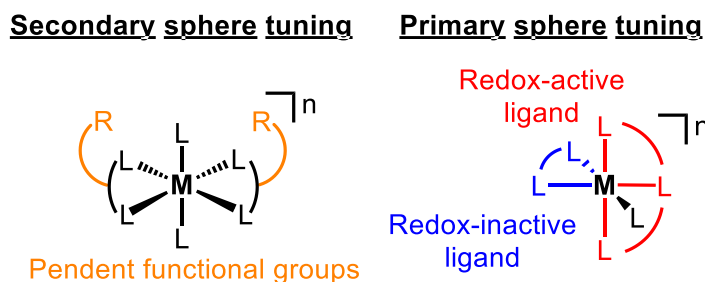


Figure 1. Approaches to reduce the overpotential in molecular CO₂ electroreduction catalysts.

Ruthenium complexes based on 2,2':6',2''-terpyridine (tpy) are prototypical examples of independent tuning in the primary coordination sphere. Moving from bipyridine to NHC-containing bidentate ligands (NHC is an N-heterocyclic carbene) leads to a dramatic increase in activity while lowering the overpotential required to maximize rate (Figure 2).^{21–23} We recently extended the complementary ligand tuning design principles to the Fe analogues.²⁴ The catalyst operated at an extremely low overpotential (<0.2 V at $E_{cat/2}$), but pyridine dissociation reduced the activity and necessitated a constant CO₂ flow to prevent inhibition from the CO product. Hypothesizing that avoiding pyridine hemilability could give rise to a more robust catalyst with higher activity while maintaining a low overpotential for CO₂ reduction, we set out to prepare a new iron organometallic complex with a symmetric bis(carbene) bidentate ligand (Figure 2).

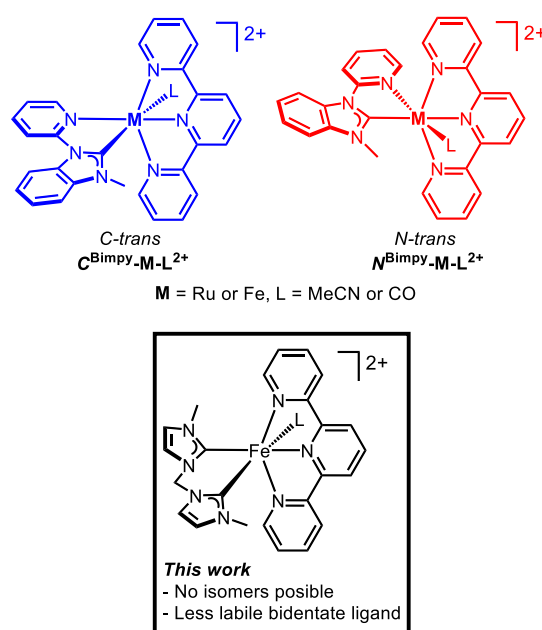


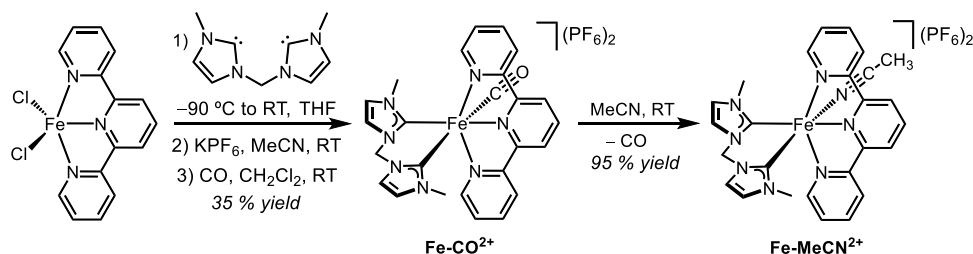
Figure 2. Previously studied Ru²² and Fe²⁴ CO₂ electrocatalysts and the new Fe complex focus of this work.

Here we report the synthesis of a new bis-carbene iron complex $[\text{Fe}(\text{tpy})(\text{bis-mim})(\text{MeCN})]^{2+}$ (bis-mim is methylenebis(*N*-methylimidazol-2-ylidene)) and demonstrate that it is a low overpotential and selective electrocatalyst for CO_2 reduction to CO. Mechanistic studies based on kinetic zone diagrams and computations indicate that CO_2 nucleophilic attack is the turnover-limiting step. Comparisons with the pyridyl-carbene analogue show how careful modification of the *primary* coordination sphere of first row transition metal electrocatalysts can be used to control the rates of chemical steps in CO_2 electroreduction without compromising the overpotential.

Results and discussion

In initial synthetic attempts, $\text{Fe}(\text{tpy})\text{Cl}_2^{25}$ was treated with free bis-mim (generated *in situ*, see the SI, Section 1.2 for details) at $-90\text{ }^\circ\text{C}$ in THF, followed by addition of KPF_6 in MeCN, resulting in a mixture that proved difficult to work with. However, replacing the N_2 atmosphere over the crude reaction mixture with CO resulted in precipitation of Fe-CO^{2+} as an orange solid in 35% yield (Scheme 1). Subsequent stirring of a solution of Fe-CO^{2+} in acetonitrile under N_2 provided the acetonitrile complex, Fe-MeCN^{2+} , in quantitative yield.

Scheme 1. Synthesis of Fe-MeCN^{2+} and Fe-CO^{2+} .



The ^1H NMR spectra of both iron complexes display the sharp and well-resolved signals expected for diamagnetic complexes in low-spin d^6 configurations. The pattern of signals is consistent with C_s molecular symmetry, indicating rapid inversion of the methylene bridge of the bis-mim ligand in solution. The two resonances corresponding to the methyl protons have quite distinct chemical shifts (4.33 and 2.61 ppm for Fe-CO^{2+} , 3.91 and 2.29 ppm for Fe-MeCN^{2+}). This can be explained in terms of the different anisotropic effect of tpy with respect to the monodentate ligand (MeCN or CO).²⁶ A similar effect was previously observed on related Ru and Fe complexes based on asymmetric Mebm-py or Mebm-pic ligands, for which the chemical shift of these protons was indicative of the isomer generated.^{22–24} Bidentate coordination of the symmetric bis-mim ligand can only produce one geometric isomer, contrasting the complexes bearing the asymmetric Mebm-py ligand. Comparisons of

spectra of the previous complexes with spectra of Fe-CO^{2+} and Fe-MeCN^{2+} established the identity of the resonance at higher field as belonging to the protons of the methyl group located close to the tpy ligand. ^{13}C NMR spectra show characteristic resonances of two distinct metallated carbene carbons (183.3 and 180.7 ppm for Fe-CO^{2+} , 195.4 and 183.5 ppm for Fe-MeCN^{2+}).

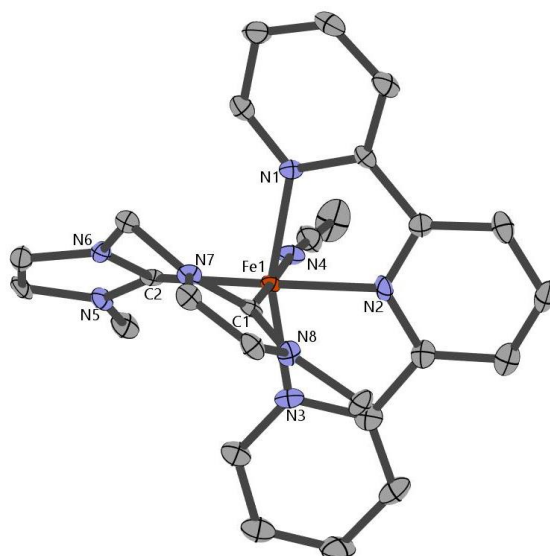


Figure 3. Structural representation of Fe-MeCN^{2+} with ellipsoids drawn at the 50% level. Hydrogen atoms and two PF_6 counterions are omitted for clarity. Selected distances (\AA) and angles (deg): $\text{Fe}(1)\text{-C}(1)$ 1.979(7), $\text{Fe}(1)\text{-C}(2)$ 1.983(7), $\text{Fe}(1)\text{-N}(1)$ 1.988(5), $\text{Fe}(1)\text{-N}(2)$ 1.897(6), $\text{Fe}(1)\text{-N}(3)$ 1.998(6) and $\text{Fe}(1)\text{-N}(4)$ 1.976(6); $\text{C}(1)\text{-Fe}(1)\text{-C}(2)$ 86.8(3), $\text{C}(1)\text{-Fe}(1)\text{-N}(4)$ 177.8(3), $\text{C}(2)\text{-Fe}(1)\text{-N}(2)$ 178.0(3), $\text{N}(1)\text{-Fe}(1)\text{-N}(3)$ 161.2(2).

The solid-state structure of Fe-MeCN^{2+} was determined by X-ray diffraction of single crystals grown by layering a MeCN solution of Fe-MeCN^{2+} with diethyl ether (Figure 3). The $\text{Fe-C}_{\text{carbene}}$ bond distance is very similar for both NHC ligands (1.979(7) and 1.983(7) \AA). The bis-mim ligand forms a six-membered metallacycle in a “boat” configuration, leading to C_1 molecular symmetry in the solid-state (vs C_s in solution).

The structure of Fe-MeCN^{2+} can be compared with the previously reported Mebim-py analogue that places the NHC *trans* to MeCN (Table 1).²⁴ The $\text{Fe-monodentate-ligand}$ bond distance in Fe-MeCN^{2+} and $\text{C}^{\text{Bimpy}}\text{-Fe-MeCN}^{2+}$ are very similar (Table 1) indicating similar *trans* influence for the NHC donor in bis-mim and in Mebim-py. However, the $\text{Fe-C}_{\text{carbene}}$ distance in Fe-MeCN^{2+} is strikingly elongated by ca. 0.05 \AA relative to $\text{C}^{\text{Bimpy}}\text{-Fe-MeCN}^{2+}$. Because of the higher donor ability of imidazolylidenes when compared to benzimidazolylidenes, the opposite trend could be expected.^{27,28} The bite angle defined by the

bis-mim ligand in **Fe-MeCN**²⁺ is 86.8(3)°, close to the ideal 90° for octahedral complexes, and ca. 6 ° larger than the bite angle of the Mebim-py analogue (Table 1).²⁴ This can be attributed to the larger and more flexible 6-membered metallacycle defined by the bis-mim ligand, when compared to the more rigid 5-membered ring established by the Mebim-py ligand. These geometric differences could help to explain the longer Fe–C_{carbene} bond in **Fe-MeCN**²⁺ relative to **C^{Bimpy}-Fe-MeCN**²⁺: shorter distances between donor atoms in rigid bidentate ligands (such as in the Mebim-py ligand) forces the ligand to be located closer to the metal center to approach the ideal 90° bite angle for octahedral geometries.²³ DFT studies reproduce the experimental trends in *trans* influence, with computed Fe–CO distances for **Fe-CO**²⁺, **C^{Bimpy}-Fe-CO**²⁺, and **N^{Bimpy}-Fe-CO**²⁺ lending additional evidence for the NHC in bis-mim complexes having a weaker *trans* influence than the NHC in Mebim-py and a stronger *trans* influence than the pyridine in Mebim-py (Table S6 in the SI).

Table 1. Characterization data of Fe bis-mim and Mebim-py complexes.²⁴

Parameter	Fe-MeCN ²⁺	Fe-CO ²⁺	C^{Bimpy}-Fe-MeCN ²⁺	N^{Bimpy}-Fe-CO ²⁺ .
Fe–C _{NHC} (Å)	1.979(7) 1.983(7)	-	1.922(5)	1.921(5)
Fe–MeCN (Å)	1.976(6)	-	1.978(4)	-
Fe–CO (Å)	-	-	-	1.774(5)
Fe–N _{tpy} (Å) ^a	1.897(6)	-	1.870(4)	1.919(4)
Bite angle (deg)	86.8(3)	-	80.76(17)	80.21(18)
ν_{CO} (cm ⁻¹)	-	2012	-	2023

^aCentral nitrogen atom of the tpy ligand

Fe-CO²⁺ undergoes rapid substitution of the CO ligand in coordinating solvents, preventing crystallization as the carbonyl complex. However, the ligand substitution of the CO was slow enough to record a strong IR band at 2012 cm⁻¹ for **Fe-CO**²⁺ in CH₃CN. The related Mebim-py complex, with a pyridine *trans* to the CO ligand (*N-trans* isomer), showed less π -backdonation to the CO ligand (Table 1). Accordingly, the bis-mim complex, **Fe-CO**²⁺, releases CO more quickly. The evolution of this process was monitored in acetonitrile by UV-vis spectroscopy, revealing the presence of two isosbestic points at 403 and 477 nm (Figure S7 in the SI), indicative of a clean reaction. The exponential decay in concentration of **Fe-CO**²⁺ points to a process which is first order in the complex (Figure S8 in the SI), with a rate constant $k_{\text{CO}} = 3.7 \cdot 10^{-2} \text{ s}^{-1}$ (Figure S9 in the SI). **N^{Bimpy}-Fe-CO**²⁺ was stable towards CO loss for 12 hours under the same conditions.

With new iron complexes in hand, we initiated electrochemical studies leading towards CO₂ electroreduction. Cyclic voltammograms (CVs) of **Fe-MeCN**²⁺ under N₂ displayed two reversible features, one oxidation and one reduction (Figure 4a and Figure S10 in the SI). The oxidation half-wave potential is +0.34 V vs Fc⁺/Fc and the peak-to-peak separation is 68 mV, suggesting a 1e⁻ process (Figure 4a).²⁹ A reduction is found at -1.65 V vs Fc⁺/Fc, with a peak current that is approximately twice that of the oxidation, consistent with a 2e⁻ process. However, the peak-to-peak separation of this wave is 140 mV, much larger than the theoretical value of 28.5 mV for a 2e⁻ reduction (standard potential of the second reduction more positive than the first one).^{30,31} On careful inspection, a shoulder is apparent in both the forward and reverse scans, implying two closely spaced 1e⁻ processes rather than a single 2e⁻ wave (Figure S10, S11 and S47a in the SI). Differential pulse voltammetry (DPV) successfully distinguished the two closely spaced reductions ($E^{\circ}(\text{Fe}^{2+/+}) = -1.61$ V and $E^{\circ}(\text{Fe}^{+/0}) = -1.67$ V vs Fc⁺/Fc, Figure 4b).

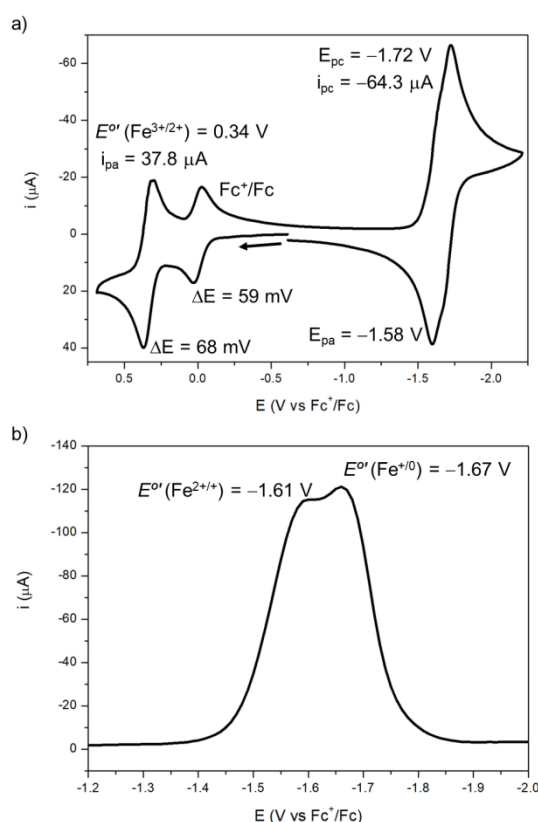


Figure 4. (a) CV of **Fe-MeCN**²⁺ in the presence of ferrocene (Fc) under N₂ atmosphere in MeCN. (b) DPV of **Fe-MeCN**²⁺ in MeCN under N₂ atmosphere. Conditions: [Fe] = 1 mM,

[TBAPF₆] = 100 mM, 3 mm glassy carbon disc working electrode, Pt wire counter electrode, Ag wire pseudoreference electrode, and 100 mV/s.

Density functional theory (DFT) computational studies were conducted using the B3LYP functional,³² 6-311+g** basis set, with implicit SMD acetonitrile solvation and Grimme-D3 dispersion correction. The DFT modelling agrees with the first reduction of **Fe-MeCN**²⁺ being ligand-centered, based on the singly occupied molecular orbital (SOMO) and the spin density of **Fe-MeCN**⁺ located on the tpy ligand (Figure 5a and 5b). The second reduction, conversely, is predominantly iron-centered. Broken symmetry calculations did not yield a lower energy solution (see supporting Information section 6.4 for details). The doubly reduced species after acetonitrile dissociation, **Fe**⁰, shows a square pyramidal geometry. All efforts to find a minimum in energy with a trigonal bipyramidal geometry converged to square pyramidal. The highest occupied molecular orbital (HOMO) of this species features a significant degree of metal character (36% located on the Fe atom, see Table S7 in the SI) with a large contribution of the tpy ligand (Figure 5c). The most stable electronic structure is a closed-shell singlet (see Section 6.4 in the SI for a discussion of the electronic configuration of **Fe**⁰), which is in contrast with the open-shell singlet configuration recently reported for a related iron polypyridine complex.³³

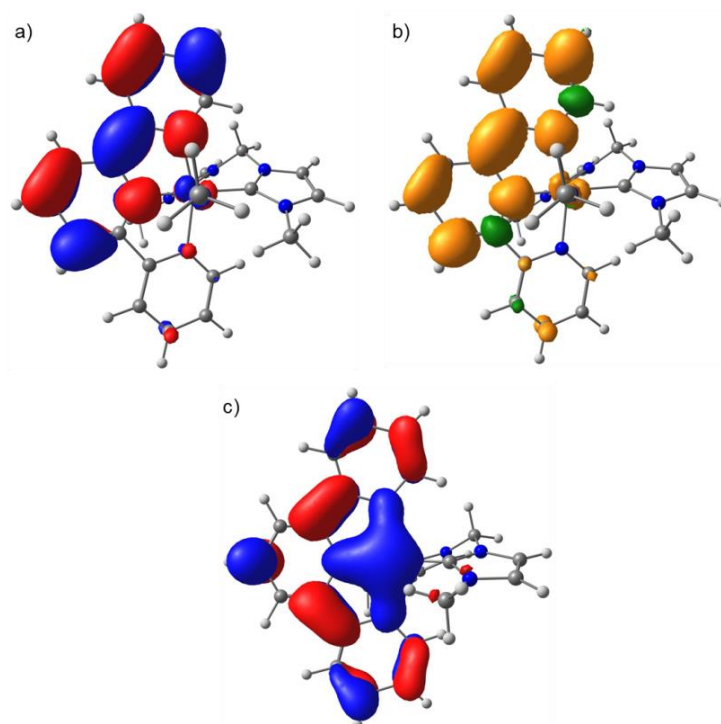


Figure 5. SOMO (a) and spin density plot (b) of **Fe-MeCN**⁺ and HOMO of **Fe**⁰ (c).

Comparisons with the previously described electrocatalyst bearing a similar ligand framework are illustrative to identify trends in their redox events. Both **Fe-MeCN²⁺** and **C^{Bimpy}-Fe-MeCN²⁺** are reduced at almost the same potential (-1.66 V and -1.61/-1.69 V vs Fc⁺/Fc, respectively, Table 2). In both cases, DFT calculations indicate that the first reduction is highly localized at the tpy ligand (around 10 % of the SOMO is centered at Fe, see Table S7 in the SI). DFT suggests that the HOMO of the doubly reduced complex, **Fe⁰**, has slightly more metal character than the analogue **C^{Bimpy}-Fe⁰** (36 % vs 21 %, see Table S7 in the SI), which may explain why the electrochemistry reveals two closely spaced 1e⁻ features rather than a single 2e⁻ feature. The metal center is also important, as the analogous Ru complexes have quite different electrochemical behavior.^{22,23,34}

Although the tpy ligand leads to Fe^{2+/+} and Fe⁺⁰ potentials being very similar for the bis-mim and Mebim-py complexes, the purely metal-centered **Fe-MeCN³⁺** reduction potential is, in contrast, cathodically shifted by nearly 300 mV relative to the reduction of the iron(III) Mebim-py complex. This large shift is expected due to the more electron rich character of the iron center supported by the highly donating bis-mim ligand. This highlights the key role of tpy in controlling electrochemical potentials, and suggests that a similar onset potential for catalysis could be expected for the two Fe complexes.

Table 2. Reduction potentials of structurally related complexes (all potentials in V vs Fc⁺/Fc)

	$E^{o'}$ (M ^{3+/2+})	$E^{o'}$ (M ^{2+/+} or M ^{2+/0})	$E^{o'}$ (M ⁺⁰)
Fe-MeCN²⁺	0.34	-1.61	-1.67
C^{Bimpy}-Fe-MeCN²⁺	0.63	-1.66	-
C^{Bimpy}-Ru-MeCN²⁺	0.86	-1.69	-1.94

To probe for electrochemical catalysis, CVs of **Fe-MeCN²⁺** in acetonitrile were conducted under N₂ in the presence of 5% (v/v) H₂O. The CVs with and without water looked essentially identical (Figure S11), indicating that **Fe-MeCN²⁺** is not rapidly protonated upon reduction and does not mediate the reduction of water to evolve H₂ under these conditions.

CVs of **Fe-MeCN²⁺** in dry acetonitrile under a CO₂ atmosphere were essentially the same as those carried out under a N₂ atmosphere (Figure 6 and Figure S12 in the SI). With only slight changes in cathodic current and almost full reversibility maintained, it is clear that there is no rapid CO₂ reduction catalysis in the absence of a proton source. Adding 5% of H₂O, however,

resulted in significant current enhancement consistent with electrocatalytic CO₂ reduction (Figure 6).

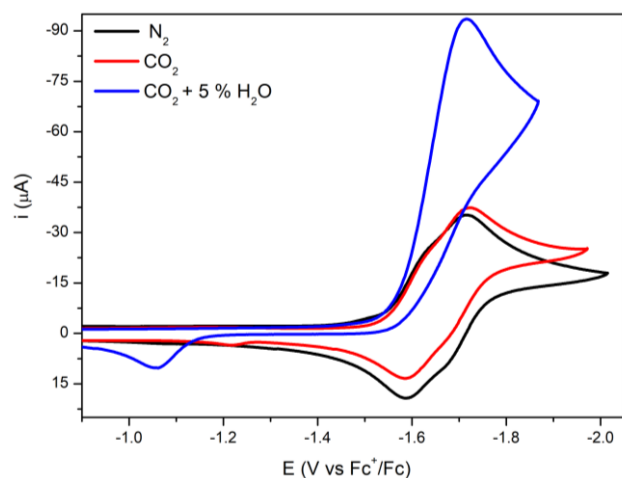


Figure 6. CV of **Fe-MeCN²⁺** under N₂ (black), CO₂ (red) and CO₂ with 5 % added H₂O (blue). Conditions: N₂ or CO₂ atmosphere, MeCN or MeCN + 5 % (v/v) H₂O, [Fe] = 1 mM, [TBAPF₆] = 100 mM, 3 mm glassy carbon disc working electrode, Pt wire counter electrode, Ag wire pseudo-reference electrode, and 100 mV/s.

In a controlled potential electrolysis (CPE) experiment, a potential of -1.75 V vs. Fc^+/Fc was applied to a solution of **Fe-MeCN²⁺** in 95/5 CH₃CN/H₂O under 1 atmosphere of CO₂, resulting in constant current over one hour (285 mC passed using a 3 mm GC disc working electrode, Figure S13 in the SI). The sole product detected in the headspace by gas chromatography was CO, in 72% Faradaic efficiency (FE). Analysis of the liquid phase by NMR spectroscopy did not reveal the production of other species. The bis-mim catalyst **Fe-MeCN²⁺** exhibits significantly higher FE for CO than the previously reported catalyst **C^{Bimpy}-Fe-MeCN²⁺** (FE(CO) = 33% under identical conditions). From the CPE data, a $k_{\text{obs}} = 9 \text{ s}^{-1}$ was obtained (see Section 4.4.1 in the SI for details), matching the activity of **C^{Bimpy}-Fe-MeCN²⁺** ($k_{\text{obs}} = 8 \text{ s}^{-1}$).

CPE experiments were undertaken under a constant flow of CO₂. Utilizing the same conditions as under batch, the FE for the generation of CO increased to 90% (Figure S14 and S15 in the SI). The current density started to decrease after 30 min of CPE, however the FE remained high at these extended electrolysis times. An increase in FE under flow was also observed in the Mebi-py analogue, although in that case the enhancement was more dramatic because the FE in batch was lower.²⁴

A scan rate dependent study was undertaken to gain insight into the mechanistic details of the reaction. At slow scan rates the CVs are peak-shaped and irreversible (Figure 7a). By

increasing the scan rate above 750 mV/s, they became S-shaped (Figure 7a), and at scan rates faster than 4 V/s the CVs commence to become peak-shaped on the forward and reverse scans (Figure 7b).

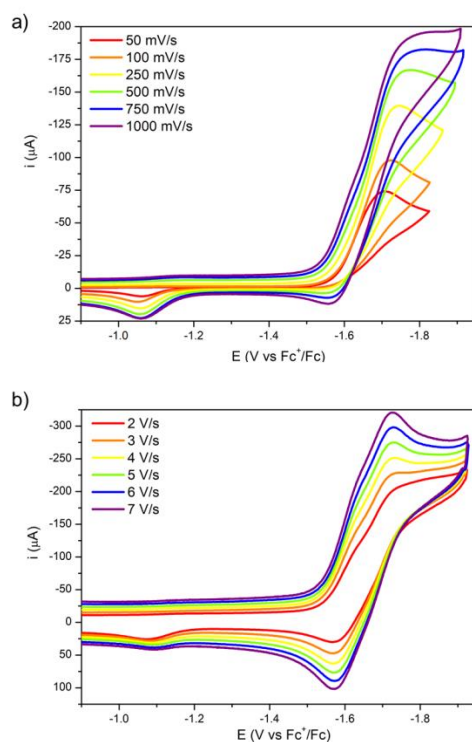





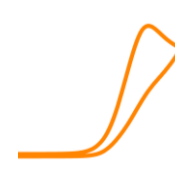




Figure 7. CVs of Fe-MeCN^{2+} from 0.05 V/s to 1 V/s (a) and from 2 V/s to 7 V/s (b) under CO_2 atmosphere with 5 % H_2O . Conditions: CO_2 atmosphere, $\text{MeCN} + 5\%$ (v/v) H_2O , $[\text{Fe}] = 1\text{ mM}$, $[\text{TBAPF}_6] = 100\text{ mM}$, 3 mm glassy carbon disc working electrode, Pt wire counter electrode, Ag wire pseudo-reference electrode.

This behavior is consistent with a catalytic system reaching three different kinetic regimes as a function of the scan rate, according to the kinetic zone diagram (Table 3).^{35,36} The peak-shaped CVs (slow scan rate) are indicative of substrate consumption and diffusion controlled catalysis (K zone). S-shaped CVs are observed when pure kinetic conditions are reached, meaning that no substrate consumption occurs at the surface of the electrode (kinetically controlled catalysis, KS zone). The catalytic current is constant for the plateau-shape CVs (from 1 to 4 V/s, Figure 8) as expected for this regime. Utilizing known equations^{36,37} (see Section 4.4.2 in the SI for details) and the plateau current of this catalytic wave, the rate constant for the turnover-limiting process step of the catalytic cycle was determined to be $k_{\text{obs}} = 59\text{ s}^{-1}$. We therefore estimate the catalytic rate constant as 34 s^{-1} , based on the average of

CV ($k_{\text{obs}} = 59 \text{ s}^{-1}$, Section 4.4.2 in the SI) and CPE ($k_{\text{obs}} = 9 \text{ s}^{-1}$, Section 4.4.1 in the SI) analysis.

The peak-shaped CVs on the forward and return sweeps at scan rates faster than 4 V/s suggest that the Fe complex is reacting with CO_2 at the timescale of the sweep. This is the expected behavior for a catalysts operating at the KD zone of the kinetic zone diagram.^{35,36} Comparison of the normalized CVs in the absence of catalysis (D zone) with those obtained in the KD zone (Table 3 and Figure S18 in the SI) show the expected shape differences for these two kinetic regimes. Another indication that KD zone is reached at fast scan rates is that the plateau current in this regime is relatively constant and similar to the current observed to the CVs of the KS zone (Figure 8).^{36,37}

Table 3. Summary of qualitative kinetic zones (for an EC process) with expected and experimental waveforms and the conditions to reach them using **Fe-MeCN²⁺**.

Zone	Expected waveform	Experimental waveform	Conditions
D			N_2 atmosphere
K			$\text{CO}_2 + 5 \% \text{ H}_2\text{O}$, $\nu < 0.75 \text{ V/s}$
KS			$\text{CO}_2 + 5 \% \text{ H}_2\text{O}$, $0.75 \text{ V/s} < \nu < 4 \text{ V/s}$
KD			$\text{CO}_2 + 5 \% \text{ H}_2\text{O}$, $\nu > 4 \text{ V/s}$

Therefore, **Fe-MeCN²⁺** is a remarkable example of a CO_2 reduction electrocatalyst which switches between three different kinetic regimes (K, KS and KD) in a very narrow scan rate window.³⁸ The crossing between kinetic zones is also evident from the representation of the catalytic current with respect the scan rate (Figure 8). Such ability is typically attributed small values of the kinetic parameter, λ .^{35,36} λ is directly proportional to the observed rate constant and inversely proportional to the scan rate of the CV ($\lambda \propto k_{\text{obs}}/\nu$). Therefore, for a catalyst to reach the KD zone, it is necessary that the scan rate of the experiment outcompetes k_{obs} .

In a catalytic cycle involving more than one chemical step, the observation of the KD zone can give insight about the nature of the turnover-limiting step of the mechanism. If the slowest step occurs after several fast chemical steps, the CVs will be irreversible at any scan rate, as the original catalyst has been chemically modified. In contrast, if the turnover-limiting step is the first chemical step after reduction, the KD zone can be achieved by outcompeting the rate constant of this chemical step. Therefore, in certain cases, the zone diagram can be utilized as an indication for the turnover-limiting step of an electrocatalysts. Thus, for **Fe-MeCN²⁺**, the scan rate study together with the zone diagram point to the CO₂ binding as the turnover-limiting step.

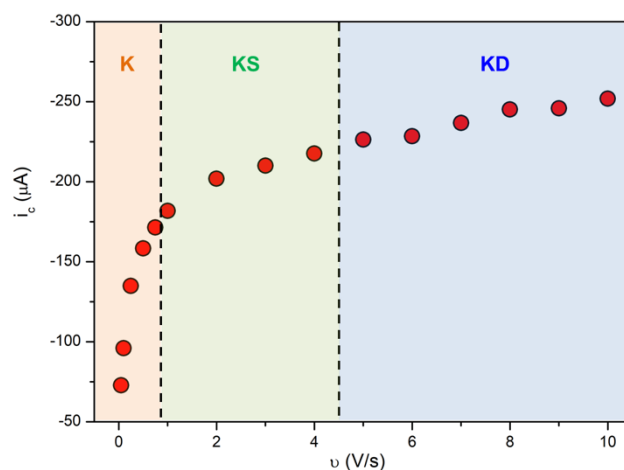


Figure 8. Evolution of the catalytic current of the CVs of Figure 7 (corrected for capacitance current) of **Fe-MeCN²⁺** with the scan rate. Kinetic zone determined from the waveform of the CV.

The overpotential required to reach half the maximum rate constant was estimated for **Fe-MeCN²⁺** as the difference between the standard potential for CO₂ reduction ($E^0_{\text{CO}_2/\text{CO}} = -1.44$ V vs Fc⁺/Fc under our conditions)³⁹ and $E_{\text{cat}/2}$ ⁴⁰ (-1.6 V vs Fc⁺/Fc): $\eta_{\text{TOF}/2} = 160$ mV. With this information, a catalytic Tafel plot can be constructed, comparing the performance of **Fe-MeCN²⁺**, **C^{Bimpy}-Fe-MeCN²⁺** and **C^{Bimpy}-Ru-MeCN²⁺** (Figure 9). The new catalyst has ca. 4-fold higher activity at the same overpotential when compared to **C^{Bimpy}-Fe-MeCN²⁺**.

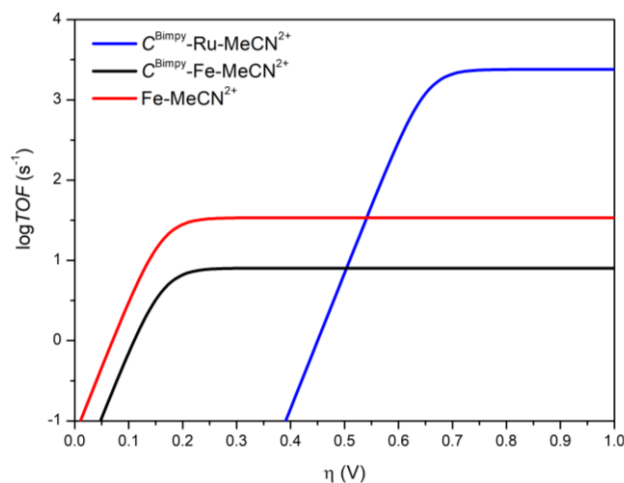


Figure 9. Catalytic Tafel Plots of $C^{\text{Bimpy}}\text{-Ru-MeCN}^{2+}$, $C^{\text{Bimpy}}\text{-Fe-MeCN}^{2+}$ and Fe-MeCN^{2+} .

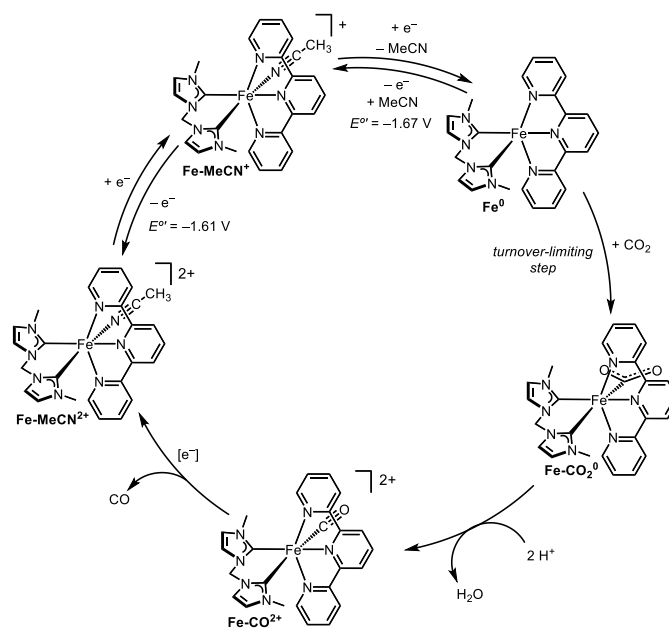
An alternative scenario which could explain reaching the KD zone would be that the first chemical step after reduction is slow, but the rate is determined by a subsequent chemical step that is even slower. Kinetic isotope effect experiments were undertaken to study this possibility. Under pure kinetic controlled conditions (fast scan rates) the solutions with D_2O and H_2O gave rise to CVs of the same plateau shape (Figures S23-S27 in the SI), indicating that the catalytic reaction encounters no kinetic isotope effect ($k_{\text{obs,H}}/k_{\text{obs,D}} = 1$). Our interpretation is that protonation is not involved in the turnover-limiting step(s) of the reaction when 5% H_2O (v/v) is present. Instead, CO_2 nucleophilic attack or CO dissociation could be limiting turnover. The CVs under CO_2 atmosphere and in the absence of protons did not show any significant difference with the electrochemistry obtained under inert atmosphere (Figure 6). This suggests that the CO_2 binding to the doubly reduced iron intermediate could be endergonic or slow, in agreement with the scan rate study. DFT calculations indicate that this step is indeed endergonic by 10.6 kcal/mol (see Section 6.7 in the SI).

The electrochemistry of Fe-CO^{2+} was studied to understand the factors governing the last step of the catalytic cycle, that is, the CO loss step. CVs under N_2 in MeCN revealed an irreversible oxidation ($E_{\text{pa}} = 0.9$ V vs Fc^+/Fc at 100 mV/s, Figure S31). A reduction feature was apparent in the return sweep, which is attributed to the $\text{Fe-MeCN}^{3+/2+}$ couple after carbonyl substitution by MeCN. CVs of Fe-CO^{2+} changed during the course of the experiments due to the CO substitution by MeCN ($k_{\text{CO}} = 3.7 \cdot 10^{-2} \text{ s}^{-1}$ *vide supra*), preventing extraction of an accurate rate constant for the oxidatively triggered CO substitution. No reductive feature attributed to the reduction of Fe-CO^{2+} could be observed even if the CV was

taken right after dissolution of the complex (Figure S32). The CV looked very similar to the one belonging to **Fe-MeCN**²⁺ even at very fast scan rates (100 V/s, Figure S33). We propose that upon one electron reduction, rapid CO loss occurs through a redox catalyzed process,^{41–43} generating **Fe-MeCN**²⁺ near the electrode surface. DFT supports the redox-catalyzed CO release hypothesis. CO dissociation from **Fe-CO**⁺ is computed to be isoenergetic ($\Delta G = 0$ kcal/mol, see Section 6.7 in the SI). A similar process was also observed for the Me-bimpy analogue.²⁴ The rapid rate of CO dissociation confirms that it cannot be the slowest step of the reaction, providing further support for Fe nucleophilic attack of CO₂ being the turnover-limiting process. The rate constant for catalysis ($k_{\text{obs}} = 34 \text{ s}^{-1}$) of **Fe-MeCN**²⁺ can be attributed to this chemical step. Similar rate constants for CO₂ binding have been reported in the literature (see Table S1 in the SI).^{44–47}

The combined experimental and computational data suggest a mechanism involving two sequential 1e⁻ reductions and acetonitrile dissociation generating five-coordinate **Fe**⁰ (Scheme 2). The subsequent nucleophilic attack to CO₂ to form a metalcarboxylate is proposed to be the turnover-limiting step. Double protonation to release H₂O and generate **Fe-CO**²⁺, which undergoes redox-catalyzed CO release under the applied potentials of catalysis to regenerate **Fe-MeCN**²⁺. The “protonation first” pathway is favored over a mechanism that involves reduction of a metalcarboxylic acid intermediate because this species is computed to have a reduction potential too negative to explain the experimental observations (see Table S10 in the SI).

Scheme 2. Proposed mechanism of CO₂ electroreduction with **Fe-MeCN**²⁺ (potentials vs Fc^{+/0}).



The gradual decrease in current over time during catalytic CPE experiments, which is tied to a decrease in the amount of CO produced, is consistent with eventual decomposition to a catalytically inactive species. While it can be challenging to understand the mechanisms of catalyst degradation, and relatively little is known about decomposition processes that occur during CO₂ reduction catalysis, such knowledge could be helpful for designing new, more robust catalysts.^{48,49} To gain insight into the nature of the catalyst deactivation, IR spectroelectrochemistry was performed under standard catalytic conditions. Application of stepwise negative potentials gave rise to an IR stretch at 1836 cm⁻¹ (Figure 10).

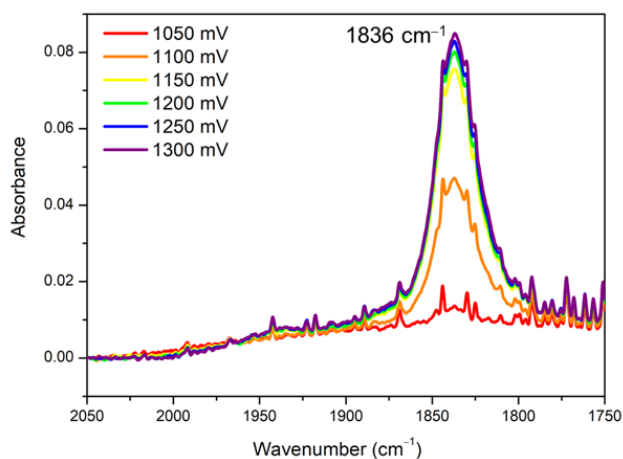


Figure 10. IR-SEC monitoring reduction of **Fe-MeCN**²⁺ with applied potentials stepped from -1050 to -1300 mV vs Ag wire pseudoreference. Conditions: CO₂ atmosphere, [Fe] = 3 mM, [TBAPF₆] = 100 mM, MeCN + 5 % H₂O, Au working electrode, Pt wire counter electrode, and Ag wire pseudoreference electrode.

The energy of this band lies at the expected range for low-valent Fe-carbonyl species, and DFT calculations indeed point to a low-valent Fe complex. The best match of computational and experimental vibrational data comes from a structure with one of the NHCs protonated ($\nu_{\text{CO}} = 1828 \text{ cm}^{-1}$ see SI for details). Therefore, protonation of NHCs during catalysis seems a likely potential decomposition pathway for NHC containing Fe electrocatalysts (Figure 11). It is interesting to point at the relatively long Fe–NHC bond length on **Fe-MeCN**²⁺ (Table 2), which may contribute this process.

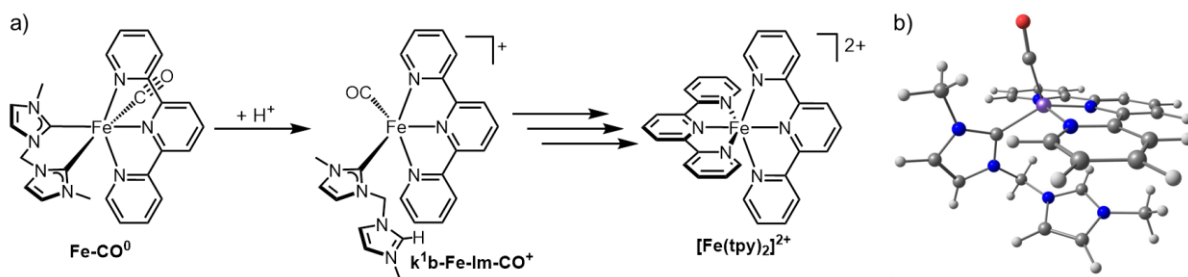


Figure 11. Protonation reaction of the low valent carbonyl intermediate (a) and DFT computed structure of the product of the reaction (b).

Inspection of the CVs under catalytic conditions reveals an oxidation feature in the reverse scan after catalysis at -1.05 V vs Fc^+/Fc (Figure 6). Multi-scan CVs of Fe-MeCN^{2+} under CO_2 atmosphere in 95/5 $\text{CH}_3\text{CN}/\text{H}_2\text{O}$ showed a reduction coupled to this oxidation (Figure 12 and Figures S34-S44). This voltammetry is distinct from that of both Fe-MeCN^{2+} and Fe-CO^{2+} . The second scan showed a catalytic wave with lower intensity than in the first sweep, suggesting the formation of an intermediate that is not a competent catalyst. The intensity of the return oxidation is higher when H_2O was utilized as proton source when compared with D_2O (Figures S19-S30 in the SI), suggesting that it is related to a protonation dependent process. This KIE gives further credence to the hypothesis that protonation of the NHC deactivates the catalyst. DFT calculations indicate that the dissociation of one of the NHC ligands from doubly reduced carbonyl intermediate Fe-CO^0 is exergonic (Figure S57 in the SI). The decoordinated NHC could then undergo facile protonation under the catalytic conditions ($\text{MeCN} + 5\%$ (v/v) H_2O), generating the species observed by IR-SEC (Figure 11). Interestingly, NHC dissociation from the singly reduced carbonyl intermediate, Fe-CO^+ , is endergonic, with CO loss instead being thermodynamically preferred (see Figure S56 in the SI). A CV acquired after CPE showed the presence of two reversible reduction waves centered -1.60 and -1.84 V vs Fc^+/Fc (Figure S45 in the SI). These features are attributed to the formation of $[\text{Fe}(\text{tpy})_2]^{2+}$ during catalysis, as we previously observed when $\text{C}^{\text{Bimpy}}\text{-Fe-MeCN}^{2+}$ was utilized as catalyst. We propose that the dechelated species eventually fully dissociates the bis-mim ligand, leading to the stable octahedral homoleptic complex in long-term electrolyses.

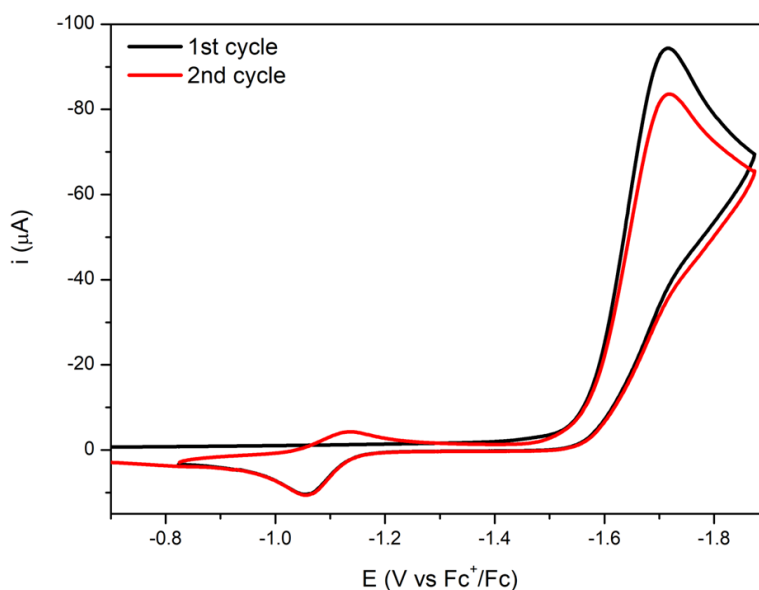


Figure 12. Multisegment CV of **Fe-MeCN²⁺** in MeCN under a CO₂ atmosphere with 5% H₂O. Conditions: CO₂ atmosphere, MeCN + 5 % H₂O, [Fe] = 1 mM, [TBAPF₆] = 100 mM, 3 mm glassy carbon disc working electrode, Pt wire counter electrode, Ag wire pseudo-reference electrode, and 100 mV/s.

Conclusions

A new iron complex based on tpy and a bis-carbene ligand (bis-mim) was synthesized and found to be a low overpotential catalyst for CO₂ electroreduction to CO with high Faradaic efficiency and a rate constant of 34 s⁻¹. The catalyst is remarkable for passing through three different kinetic regimes under catalytic conditions as a function of the scan rate. This feature allowed the nature of the turnover-limiting step to be assigned as CO₂ nucleophilic attack.

Comparisons of the current bis-mim catalyst with the previously reported pyridyl-carbene (Mebim-py) catalyst provide some guidance for future CO₂ electrocatalyst design. Both electrocatalysts show tpy-centered reductions.²²⁻²⁴ The second reduction of this type of electrocatalysts seems to be more sensitive to the type of metal and bidentate ligand. This is reflected in the reversible 2e⁻ reduction process for **C^{Bimpy}-Fe-MeCN²⁺** and the closely separated pair of reversible 1e⁻ reductions for **Fe-MeCN²⁺**, all lying at similar potentials. Despite the presence of two strongly donating NHC ligands in **Fe-MeCN²⁺**, the reduction potentials are within 50 mV of the complex with only one NHC, **C^{Bimpy}-Fe-MeCN²⁺**. As a result, **Fe-MeCN²⁺** is a faster CO-selective electrocatalyst ($k_{\text{obs}} = 34 \text{ s}^{-1}$ vs $k_{\text{obs}} = 8 \text{ s}^{-1}$) at the

same overpotential. This is noteworthy because most catalyst systems exhibit a trade-off where higher activity comes at the expense of higher overpotential.^{15,50}

Mechanistically, both electrocatalysts operate through a “protonation first” pathway, but differ in the nature of the turnover-limiting step. For **C^{Bimpy}-Fe-MeCN²⁺**, CO loss is turnover limiting, while for **Fe-MeCN²⁺** is the nucleophilic attack to CO₂. Slow CO loss from the Mebim-py complex is attributed to facile pyridine dissociation that produces an iron carbonyl complex that resists CO release. Analogous dissociation of NHC is not expected in the catalytic cycle, leading to enhanced CO release. As such, under batch conditions **Fe-MeCN²⁺** provides higher FE for CO than **C^{Bimpy}-Fe-MeCN²⁺** (72% vs 33%). Eventually an NHC ligand in the bis-mim catalyst does dissociate, though, first producing a low-valent five-coordinate Fe-CO complex and eventually producing [Fe(tpy)₂]²⁺. The NHC dissociation process is irreversible, while for the catalyst bearing Mebim-py, protonation does not occur, becoming an hemilabile ligand, which can re-bind the pyridyl donor when the concentration of CO is low.

This study shows that the *primary* coordination sphere of Fe catalysts can be tuned to control the rate of different chemical steps in CO₂ electroreduction to CO while keeping a low overpotential. The redox active tpy ligand governs the reduction process, while the bidentate ligand can be changed to fine-tune the rates of chemical step(s) in the mechanism without influencing the overpotential. This knowledge will inspire new catalysts designs in the CO₂ electroreduction arena.

Supporting information

Experimental details, NMR spectra, electrochemical methods, crystallographic methods, and computational methods (PDF)

Coordinates of computational output files (PDF)

Crystallographic data (CIF)

Acknowledgements

The synthesis, voltammetry, and spectroelectrochemistry were supported as part of the Alliance for Molecular PhotoElectrode Design for Solar Fuels (AMPED), an Energy Frontier Research Center (EFRC) funded by the U.S. Department of Energy, Office of Science, Office of Basic Energy Sciences under Award Number DE-SC0001011. Jordi Benet assisted with

crystallographic data collection. Brandie M. Ehrmann assisted with mass spectrometry. The mass spectrometry work was supported by the National Science Foundation under Grant No. (CHE-1726291). Computational studies, flow electrolyses and X-ray diffraction studies were supported by the European Commission for the ERC-CoG-2015-648304 project and the Spanish Ministry of Science for the project PID2019-110050RB-I00 (J.Ll.-F). S.G. thanks the EU for Horizon 2020 Marie Skłodowska-Curie Fellowship (Grant No.794119, Fe-RedOx-Cat).

References

- (1) Boutin, E.; Merakeb, L.; Ma, B.; Boudy, B.; Wang, M.; Bonin, J.; Anxolabéhère-Mallart, E.; Robert, M. Molecular Catalysis of CO₂ Reduction: Recent Advances and Perspectives in Electrochemical and Light-Driven Processes with Selected Fe, Ni and Co Aza Macrocyclic and Polypyridine Complexes. *Chem. Soc. Rev.* **2020**, *49* (16), 5772–5809. <https://doi.org/10.1039/D0CS00218F>.
- (2) Franco, F.; Rettenmaier, C.; Jeon, H. S.; Roldan Cuenya, B. Transition Metal-Based Catalysts for the Electrochemical CO₂ Reduction: From Atoms and Molecules to Nanostructured Materials. *Chem. Soc. Rev.* **2020**, *49* (19), 6884–6946. <https://doi.org/10.1039/D0CS00835D>.
- (3) Franco, F.; Fernández, S.; Lloret-Fillol, J. Advances in the Electrochemical Catalytic Reduction of CO₂ with Metal Complexes. *Curr. Opin. Electrochem.* **2019**, *15*, 109–117. <https://doi.org/10.1016/j.coelec.2019.04.002>.
- (4) Francke, R.; Schille, B.; Roemelt, M. Homogeneously Catalyzed Electroreduction of Carbon Dioxide—Methods, Mechanisms, and Catalysts. *Chem. Rev.* **2018**, *118* (9), 4631–4701. <https://doi.org/10.1021/acs.chemrev.7b00459>.
- (5) Gonell, S.; Miller, A. J. M. Carbon Dioxide Electroreduction Catalyzed by Organometallic Complexes. In *Advances in Organometallic Chemistry*; Elsevier Inc., 2018; Vol. 70, pp 1–69. <https://doi.org/10.1016/bs.adomc.2018.07.001>.
- (6) Ren, S.; Joulié, D.; Salvatore, D.; Torbensen, K.; Wang, M.; Robert, M.; Berlinguette, C. P. Molecular Electrocatalysts Can Mediate Fast, Selective CO₂ Reduction in a Flow Cell. *Science*. **2019**, *365* (6451), 367–369. <https://doi.org/10.1126/science.aax4608>.
- (7) Jiang, C.; Nichols, A. W.; Machan, C. W. A Look at Periodic Trends in D-Block Molecular Electrocatalysts for CO₂ Reduction. *Dalt. Trans.* **2019**, *48* (26), 9454–9468. <https://doi.org/10.1039/C9DT00491B>.
- (8) Amanullah, S.; Saha, P.; Nayek, A.; Ahmed, M. E.; Dey, A. Biochemical and Artificial Pathways for the Reduction of Carbon Dioxide, Nitrite and the Competing Proton Reduction: Effect of 2nd Sphere Interactions in Catalysis. *Chem. Soc. Rev.* **2021**, *50* (6), 3755–3823. <https://doi.org/10.1039/D0CS01405B>.
- (9) Nichols, A. W.; Machan, C. W. Secondary-Sphere Effects in Molecular Electrocatalytic CO₂ Reduction. *Front. Chem.* **2019**, *7*, 1–19. <https://doi.org/10.3389/fchem.2019.00397>.

- (10) Stratakes, B. M.; Dempsey, J. .; Miller, A. J. . Determining the Overpotential of Electrochemical Fuel Synthesis Mediated by Molecular Catalysts: Recommended Practices, Standard Reduction Potentials, and Challenges. *ChemElectroChem* **2021**. <https://doi.org/10.1002/celec.202100576>.
- (11) Helm, M. L.; Stewart, M. P.; Bullock, R. M.; DuBois, M. R.; DuBois, D. L. A Synthetic Nickel Electrocatalyst with a Turnover Frequency Above 100,000 s⁻¹ for H₂ Production. *Science*. **2011**, *333* (6044), 863–866. <https://doi.org/10.1126/science.1205864>.
- (12) Shaw, W. J.; Helm, M. L.; Du Bois, D. L. A Modular, Energy-Based Approach to the Development of Nickel Containing Molecular Electrocatalysts for Hydrogen Production and Oxidation. *Biochim. Biophys. Acta - Bioenerg.* **2013**, *1827* (8–9), 1123–1139. <https://doi.org/10.1016/j.bbambio.2013.01.003>.
- (13) Costentin, C.; Savéant, J.-M. Towards an Intelligent Design of Molecular Electrocatalysts. *Nat. Rev. Chem.* **2017**, *1* (11), 0087. <https://doi.org/10.1038/s41570-017-0087>.
- (14) Costentin, C.; Drouet, S.; Robert, M.; Savéant, J.-M. A Local Proton Source Enhances CO₂ Electroreduction to CO by a Molecular Fe Catalyst. *Science*. **2012**, *338* (6103), 90–94. <https://doi.org/10.1126/science.1224581>.
- (15) Azcarate, I.; Costentin, C.; Robert, M.; Savéant, J.-M. Through-Space Charge Interaction Substituent Effects in Molecular Catalysis Leading to the Design of the Most Efficient Catalyst of CO₂-to-CO Electrochemical Conversion. *J. Am. Chem. Soc.* **2016**, *138* (51), 16639–16644. <https://doi.org/10.1021/jacs.6b07014>.
- (16) Ngo, K. T.; McKinnon, M.; Mahanti, B.; Narayanan, R.; Grills, D. C.; Ertem, M. Z.; Rochford, J. Turning on the Protonation-First Pathway for Electrocatalytic CO₂ Reduction by Manganese Bipyridyl Tricarbonyl Complexes. *J. Am. Chem. Soc.* **2017**, *139* (7), 2604–2618. <https://doi.org/10.1021/jacs.6b08776>.
- (17) Roy, S.; Sharma, B.; Pécaut, J.; Simon, P.; Fontecave, M.; Tran, P. D.; Derat, E.; Artero, V. Molecular Cobalt Complexes with Pendant Amines for Selective Electrocatalytic Reduction of Carbon Dioxide to Formic Acid. *J. Am. Chem. Soc.* **2017**, *139* (10), 3685–3696. <https://doi.org/10.1021/jacs.6b11474>.
- (18) Talukdar, K.; Sinha Roy, S.; Amatya, E.; Sleeper, E. A.; Le Magueres, P.; Jurss, J. W. Enhanced Electrochemical CO₂ Reduction by a Series of Molecular Rhenium Catalysts Decorated with Second-Sphere Hydrogen-Bond Donors. *Inorg. Chem.* **2020**, *59* (9), 6087–6099. <https://doi.org/10.1021/acs.inorgchem.0c00154>.
- (19) Nichols, A. W.; Hooe, S. L.; Kuehner, J. S.; Dickie, D. A.; Machan, C. W. Electrocatalytic CO₂ Reduction to Formate with Molecular Fe(III) Complexes Containing Pendent Proton Relays. *Inorg. Chem.* **2020**, *59* (9), 5854–5864. <https://doi.org/10.1021/acs.inorgchem.9b03341>.
- (20) Roy, S. S.; Talukdar, K.; Jurss, J. W. Electro- and Photochemical Reduction of CO₂ by Molecular Manganese Catalysts: Exploring the Positional Effect of Second-Sphere Hydrogen-Bond Donors. *ChemSusChem* **2021**, *14* (2), 662–670. <https://doi.org/10.1002/cssc.202001940>.

- (21) Chen, Z.; Chen, C.; Weinberg, D. R.; Kang, P.; Concepcion, J. J.; Harrison, D. P.; Brookhart, M. S.; Meyer, T. J. Electrocatalytic Reduction of CO₂ to CO by Polypyridyl Ruthenium Complexes. *Chem. Commun.* **2011**, 47 (47), 12607. <https://doi.org/10.1039/c1cc15071e>.
- (22) Gonell, S.; Massey, M. D.; Moseley, I. P.; Schauer, C. K.; Muckerman, J. T.; Miller, A. J. M. The Trans Effect in Electrocatalytic CO₂ Reduction: Mechanistic Studies of Asymmetric Ruthenium Pyridyl-Carbene Catalysts. *J. Am. Chem. Soc.* **2019**, 141 (16), 6658–6671. <https://doi.org/10.1021/jacs.9b01735>.
- (23) Gonell, S.; Assaf, E. A.; Duffee, K. D.; Schauer, C. K.; Miller, A. J. M. Kinetics of the Trans Effect in Ruthenium Complexes Provide Insight into the Factors That Control Activity and Stability in CO₂ Electroreduction. *J. Am. Chem. Soc.* **2020**, 142 (19), 8980–8999. <https://doi.org/10.1021/jacs.0c02912>.
- (24) Gonell, S.; Lloret-Fillol, J.; Miller, A. J. M. An Iron Pyridyl-Carbene Electrocatalyst for Low Overpotential CO₂ Reduction to CO. *ACS Catal.* **2021**, 11 (2), 615–626. <https://doi.org/10.1021/acscatal.0c03798>.
- (25) Delis, J. G. P.; Chirik, P. J.; Tondreau, A. M. Hydrosilylation Catalysts. U.S. Patent, US 2011/0009565A1, 2011.
- (26) Camp, A. M.; Kita, M. R.; Grajeda, J.; White, P. S.; Dickie, D. A.; Miller, A. J. M. Mapping the Binding Modes of Hemilabile Pincer–Crown Ether Ligands in Solution Using Diamagnetic Anisotropic Effects on NMR Chemical Shift. *Inorg. Chem.* **2017**, 56 (18), 11141–11150. <https://doi.org/10.1021/acs.inorgchem.7b01485>.
- (27) Dröge, T.; Glorius, F. The Measure of All Rings--N-Heterocyclic Carbenes. *Angew. Chem. Int. Ed.* **2010**, 49 (39), 6940–6952. <https://doi.org/10.1002/anie.201001865>.
- (28) Nelson, D. J.; Nolan, S. P. Quantifying and Understanding the Electronic Properties of N-Heterocyclic Carbenes. *Chem. Soc. Rev.* **2013**, 42 (16), 6723. <https://doi.org/10.1039/c3cs60146c>.
- (29) Elgrishi, N.; Rountree, K. J.; McCarthy, B. D.; Rountree, E. S.; Eisenhart, T. T.; Dempsey, J. L. A Practical Beginner's Guide to Cyclic Voltammetry. *J. Chem. Educ.* **2018**, 95 (2), 197–206. <https://doi.org/10.1021/acs.jchemed.7b00361>.
- (30) Tulyathan, B.; Geiger, W. E. Structural Consequences of Electron-Transfer Reactions. Part 12. Multi Electron Processes Involving Structural Changes. The Two-Electron Reduction of Hexaosmium Carbonyl Cluster (Os₆(CO)₁₈). *J. Am. Chem. Soc.* **1985**, 107 (21), 5960–5967. <https://doi.org/10.1021/ja00307a022>.
- (31) Sampson, M. D.; Nguyen, A. D.; Grice, K. A.; Moore, C. E.; Rheingold, A. L.; Kubiak, C. P. Manganese Catalysts with Bulky Bipyridine Ligands for the Electrocatalytic Reduction of Carbon Dioxide: Eliminating Dimerization and Altering Catalysis. *J. Am. Chem. Soc.* **2014**, 136 (14), 5460–5471. <https://doi.org/10.1021/ja501252f>.
- (32) Becke, A. D. Density-functional Thermochemistry. III. The Role of Exact Exchange. *J. Chem. Phys.* **1993**, 98 (7), 5648–5652. <https://doi.org/10.1063/1.464913>.
- (33) Derrick, J. S.; Loipersberger, M.; Chatterjee, R.; Iovan, D. A.; Smith, P. T.; Chakarawet, K.; Yano, J.; Long, J. R.; Head-Gordon, M.; Chang, C. J. Metal–Ligand Cooperativity via Exchange Coupling Promotes Iron- Catalyzed Electrochemical CO₂

- Reduction at Low Overpotentials. *J. Am. Chem. Soc.* **2020**, *142* (48), 20489–20501. <https://doi.org/10.1021/jacs.0c10664>.
- (34) Chen, Z.; Chen, C.; Weinberg, D. R.; Kang, P.; Concepcion, J. J.; Harrison, D. P.; Brookhart, M. S.; Meyer, T. J. Electrocatalytic Reduction of CO₂ to CO by Polypyridyl Ruthenium Complexes. *Chem. Commun.* **2011**, *47* (47), 12607–12609. <https://doi.org/10.1039/c1cc15071e>.
- (35) Savéant, J.-M. *Elements of Molecular and Biomolecular Electrochemistry*; John Wiley & Sons, Inc: Hoboken, New Jersey, 2006; pp 96–102.
- (36) Rountree, E. S.; McCarthy, B. D.; Eisenhart, T. T.; Dempsey, J. L. Evaluation of Homogeneous Electrocatalysts by Cyclic Voltammetry. *Inorg. Chem.* **2014**, *53* (19), 9983–10002. <https://doi.org/10.1021/ic500658x>.
- (37) Walden, A. G.; Miller, A. J. M. Rapid Water Oxidation Electrocatalysis by a Ruthenium Complex of the Tripodal Ligand Tris(2-Pyridyl)Phosphine Oxide. *Chem. Sci.* **2015**, *6* (4), 2405–2410. <https://doi.org/10.1039/C5SC00032G>.
- (38) Martin, D. J.; McCarthy, B. D.; Rountree, E. S.; Dempsey, J. L. Qualitative Extension of the EC' Zone Diagram to a Molecular Catalyst for a Multi-Electron, Multi-Substrate Electrochemical Reaction. *Dalt. Trans.* **2016**, *45* (24), 9970–9976. <https://doi.org/10.1039/C6DT00302H>.
- (39) Matsubara, Y. Standard Electrode Potentials for the Reduction of CO₂ to CO in Acetonitrile–Water Mixtures Determined Using a Generalized Method for Proton-Coupled Electron-Transfer Reactions. *ACS Energy Lett.* **2017**, *2* (8), 1886–1891. <https://doi.org/10.1021/acsenergylett.7b00548>.
- (40) Appel, A. M.; Helm, M. L. Determining the Overpotential for a Molecular Electrocatalyst. *ACS Catal.* **2014**, *4* (2), 630–633. <https://doi.org/10.1021/cs401013v>.
- (41) Kochi, J. K. Electron Transfer and Transient Radicals in Organometallic Chemistry. *J. Organomet. Chem.* **1986**, *300* (1–2), 139–166. [https://doi.org/10.1016/0022-328X\(86\)84060-8](https://doi.org/10.1016/0022-328X(86)84060-8).
- (42) Astruc, D. Electron-Transfer Chain Catalysis in Organotransition Metal Chemistry. *Angew. Chem. Int. Ed.* **1988**, *27* (5), 643–660. <https://doi.org/10.1002/anie.198806431>.
- (43) Grice, K. A.; Gu, N. X.; Sampson, M. D.; Kubiak, C. P. Carbon Monoxide Release Catalysed by Electron Transfer: Electrochemical and Spectroscopic Investigations of [Re(Bpy-R)(CO)₄](OTf) Complexes Relevant to CO₂ Reduction. *Dalt. Trans.* **2013**, *42* (23), 8498. <https://doi.org/10.1039/c3dt50612f>.
- (44) Cometto, C.; Chen, L.; Lo, P.-K.; Guo, Z.; Lau, K.-C.; Anxolabéhère-Mallart, E.; Fave, C.; Lau, T.-C.; Robert, M. Highly Selective Molecular Catalysts for the CO₂-to-CO Electrochemical Conversion at Very Low Overpotential. Contrasting Fe vs Co Quaterpyridine Complexes upon Mechanistic Studies. *ACS Catal.* **2018**, *8* (4), 3411–3417. <https://doi.org/10.1021/acscatal.7b04412>.
- (45) Fernández, S.; Franco, F.; Casadevall, C.; Martin-Diaconescu, V.; Luis, J. M.; Lloret-Fillol, J. A Unified Electro- and Photocatalytic CO₂ to CO Reduction Mechanism with Aminopyridine Cobalt Complexes. *J. Am. Chem. Soc.* **2020**, *142* (1), 120–133. <https://doi.org/10.1021/jacs.9b06633>.

- (46) Creutz, C.; Schwarz, H. A.; Wishart, J. F.; Fujita, E.; Sutin, N. Thermodynamics and Kinetics of Carbon Dioxide Binding to Two Stereoisomers of a Cobalt(I) Macrocycle in Aqueous Solution. *J. Am. Chem. Soc.* **1991**, *113* (9), 3361–3371. <https://doi.org/10.1021/ja00009a022>.
- (47) Smieja, J. M.; Benson, E. E.; Kumar, B.; Grice, K. A.; Seu, C. S.; Miller, A. J. M.; Mayer, J. M.; Kubiak, C. P. Kinetic and Structural Studies, Origins of Selectivity, and Interfacial Charge Transfer in the Artificial Photosynthesis of CO. *Proc. Natl. Acad. Sci.* **2012**, *109* (39), 15646–15650. <https://doi.org/10.1073/pnas.1119863109>.
- (48) Artero, V.; Fontecave, M. Solar Fuels Generation and Molecular Systems: Is It Homogeneous or Heterogeneous Catalysis? *Chem. Soc. Rev.* **2013**, *42*, 2338–2356. <https://doi.org/10.1039/C2CS35334B>.
- (49) Lee, K. J.; McCarthy, B. D.; Dempsey, J. L. On Decomposition, Degradation, and Voltammetric Deviation: The Electrochemist's Field Guide to Identifying Precatalyst Transformation. *Chem. Soc. Rev.* **2019**, *48* (11), 2927–2945. <https://doi.org/10.1039/C8CS00851E>.
- (50) Dey, S.; Ahmed, M. E.; Dey, A. Activation of Co(I) State in a Cobalt-Dithiolato Catalyst for Selective and Efficient CO₂ Reduction to CO. *Inorg. Chem.* **2018**, *57* (10), 5939–5947. <https://doi.org/10.1021/acs.inorgchem.8b00450>.